Design of hybrid protein-coated magnetic core-mesoporous silica shell nanocomposites for MRI and drug release assessed in a 3D tumor cell model

Mathilde Ménard, Florent Meyer, Christine Affolter-Zbaraszczuk, Morgane Rabineau, Alexandre Adam, Paula Duenas Ramirez, Sylvie Bégin-Colin, Damien Mertz

Design of hybrid protein-coated magnetic core-mesoporous silica shell nanocomposites for MRI and drug release assessed in a 3D tumor cell model

Mathilde Ménard[1,2], Florent Meyer[2,*], Christine Affolter-Zbaraszczuk[2], Morgane Rabineau[2], Alexandre Adam[1], Paula Duenas Ramirez[1], Sylvie Bégin-Colin[1,*] and Damien Mertz[1,*]

[1]*Institut de Physique et Chimie des Matériaux de Strasbourg (IPCMS), UMR 7504, CNRS, Université de Strasbourg, 23, rue du Loess, BP 43, 67034 Strasbourg, France. E-mails: damien.mertz@ipcms.unistra.fr, sylvie.begin@ipcms.unistra.fr*

[2]*Université de Strasbourg, INSERM, UMR_S 1121 Biomatériaux et bioingénierie, FMTS, 11 rue Humann, 67085 Strasbourg, Cedex, France. E-mail : fmeyer@unistra.fr*

ABSTRACT

In this work, we describe the design and the use of a novel theranostic hybrid nanocomposite made of an iron oxide core and a mesoporous silica shell (IO@MS) of ca. 30 nm coated by human serum albumin (HSA) layer for magnetic resonance imaging (MRI) and drug delivery applications. The porosity of IO@MS nanoparticles was loaded with an antitumoral drug, Doxorubicin (Dox) reaching a high drug loading capacity (DLC) of 34w%. To entrap the drug, a tight HSA coating held via *iso*butyramide (IBAM) binders was deposited. We show that this protein nanoassembly entraps the drugs efficiently and behaves as an innovative enzyme-sensitive gatekeeper that is degraded upon protease action. Finally we assess the Dox release in a 3D cell model via confocal imaging and its cytotoxicity is shown by growth inhibition studies on liver cancer cell spheroids.

INTRODUCTION

The blossoming growth of nanotechnologies has brought rapid progress in the design of multifunctional nanoplatforms called “nanotheranostics” which combine diagnosis and targeted therapy.[1–3] Among functional nanoparticles (NPs) for theranostic applications, superparamagnetic iron oxide nanoparticles (IO NPs) are of particular interest. Such NPs, apart from there magnetic resonance imaging (MRI) properties are currently emerging as powerful

nano-heating mediators for magnetic hyperthermia making them nanotheranostic platforms by themselves.[4–7] Moreover, various organic or inorganic coatings[8,9] have been investigated to allow drug loading, furtivity and/or targeting ability to address treatment side effect issues. The design of magnetic nanoplatforms with drug delivery capability through local or remote stimuli is therefore of outmost importance because of high expectations raised by synergistic combined therapies.[10–14]

Organic molecules or polymer nanocoatings at the surface of IO NPs can be used for the loading and release of drugs. The drug can be bound either via covalent or non-covalent ways to the NPs. Non covalent binding of the drug is typically achieved through electrostatic or H-bonding established with organic anchors/polymers at the NP surface and the drug release from the NPs is usually obtained through pH-conformational changes of such nanocoatings.[15,16] The main limitations of such approaches are in the low drug loading capacity (DLC) associated with a non-negligible drug leakage through the NPs coatings. Alternatively, covalent binding of the drugs to NPs that can be cleaved upon various local or external stimuli were investigated [17,18] to afford smart responses and few leaking. However, drug payload per particle is usually there rather moderate when using such strategy and the drug/nanoparticle ratio is a key parameter in the toxicity evaluation.

Inorganic coatings like mesoporous silica (MS) tend to overcome this issue as they allow, in comparison with organic coatings, higher DLC. MS NPs (without magnetic/plasmonic core) were reported reaching up to 30-48% DLC.[19,20] However such NPs must be associated with an external organic/polymer coating acting as a gatekeeper to avoid spontaneous drug release. Different strategies can be used depending on the stimulus (pH, redox, temperature) to trigger drug release. For example, Yuan et al. made use of poly(acrylic acid) polymer hydrogel grafted on MS to ensure the pH-responsive release of doxorubicin (Dox), a chemotherapeutic agent, triggered when pH was lowered from pH=7.4 to 5.6. [19] In another work, Duguet and coworkers used a thermo-sensitive lipidic-based gatekeeper to encapsulate Dox in IO@MS NPs and release it upon lipid phase melting above 40°C.[21]

Among biological stimuli, drug release ensured through enzyme biodegradation/conversion action is of particular interest. In fact, *in vivo*, enzyme expression is specifically located either in the cell surrounding or inside the cell in subcellular compartments. Such strategy was usually investigated on drug releasing polymer films coated on planar surfaces.[22–24] However, to the best of our knowledge, the design of biodegradable gatekeeper shell releasing drugs initially embedded within porous nanomaterials upon protease action is not yet reported. Furthermore, among the diversity of polymer nanocoating approaches that may be used to encapsulate drugs,

we developed the use of isobutyramide (IBAM) grafts and its derivatives as an innovative way to form non-covalent biofunctional and tight nanoassemblies.[25–28] Using such strategy, we successfully formulated self-supported protein-based hollow microcapsules and NPs. The formation of tight IBAM-HSA coatings over magnetic mesoporous silica may be thus of particular interest to design responsive coatings acting as drug gatekeepers using enzymatic degradation as stimulus to release the drugs.

Herein, we report the design of hybrid protein-coated magnetic core-mesoporous silica shell nanocomposites for MRI and drug release assessed. As described in **Figure1**, our strategy consists in building a thin mesoporous silica (MS) shell (pores of 3 nm) around superparamagnetic IO NPs, obtained by thermal decomposition. This synthesis leads to uniform and individual magnetic core covered by MS shell, called IO@MS NPs. Then, after surface modification with aminopropyltriethoxysilane (APTS), Dox is loaded by simple soaking into the porosities of the silica shell. HSA is then deposited on the silica shell surface, which is previously modified with IBAM binders. The so-obtained final system is called IO@MS-Dox-HSA. In this study, we report: i) the synthesis process and the deep characterization of the IO@MS-HSA NPs, ii) the evaluation of the contrast efficiency for MRI especially in T_2-weighted MRI, iii) the investigation of the Dox loading procedure, iv) the biological studies with a 3D model called multicellular tumor spheroid (MCTS). Finally, HSA biodegradation and subsequent Dox release is assessed by incubation of the nanocomposites in a protease media and *in vitro* in a 3D cancer cell model.

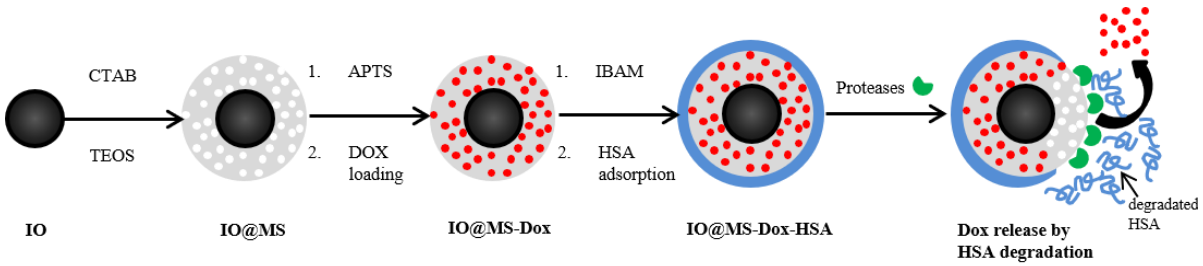

Figure 1: Schematic illustration of the synthetic procedure for IO@MS-Dox-HSA NPs and the Dox release by HSA degradation via proteases action

MATERIALS AND METHODS

Chemicals. Iron stearate (9.47% Fe), oleic acid (99%), dioctyl ether (97%) were respectively obtained from Strem Chemicals, Alfa-Aesar and Fluka. Tetraethyl orthosilicate (TEOS), ammonium hydroxide solution (25%), 3-Aminopropyltriethoxysilane (APTS), *iso*butyrylchloride (IBC), ethanol (EtOH), *N*,*N*-dimethylformamide (DMF), dimethylsulfoxide (DMSO), triethylamine

(Et3N), fluorescein *iso*thiocyanate (FITC), sodium hydrogenocarbonate ($NaHCO_3$), human serum albumin (HSA) and proteases from Streptomyces griseus were obtained from Sigma-Aldrich (France). Doxorubicin hydrochloride (Dox, purity 99%) was purchased from OChem Inc. (Des Plaines, IL) and cetyltrimethylammonium bromide (CTAB) from Roth (France).

Synthesis of spherical IO NPs by thermal decomposition method. Uniform 10 nm sized Fe_3O_4 nanocrystals were synthesized using a previously reported method.[29] Briefly 1.38 g (2.22 mmol) of iron stearate was thermally decomposed in dioctylether (20 mL) in presence of 1.25 g (4.44 mmol) of oleic acid. First the mixture was heated to 130 °C under stirring for 1 h to dissolve the reactants and remove water residues. Then by applying a heating rate of 5 °C/min the solution reached the boiling temperature (ca 287 °C) and was kept under reflux for 2 h. After washing the final product by centrifugation with a mixture of chloroform/acetone (1/3) the IO NPs stabilized with oleic acid were dispersed in chloroform with a concentration of 2 mg Fe ·mL^{-1} measured by inductively coupled plasma atomic emission spectroscopy (ICP-AES).

Coating of small pore MS around IO NPs. The MS coating method was adapted from previous reported methods.[30,31] The procedure described below is the typical procedure to synthesize IO@MS NPs of 30 nm in size and with a core of 10 nm.

First an aqueous solution of CTAB at 28 mM was prepared (500 mg in 50 mL of Milli-Q water). After complete dissolution of CTAB, 3 mL of IO NPs dispersed at 2 mg Fe/mL were added under vigorous magnetic stirring for 30 min. At this step a brown turbid solution was obtained. Then the mixture was heated up to 65°C and maintained at this temperature for 10 min under stirring to evaporate the chloroform. The solution obtained was black and transparent. A solution of 150 mL of Milli-Q water and 60 µL of a 2M NaOH solution were added to the mixture. The so obtained solution was heated up to 70°C under vigorous stirring. 1.5 mL of TEOS and 2.55 mL of EtOAc were added and this final mixture was stirred for 3h at 70°C. The particles were then washed 3 times in ethanol by centrifugation.

Silanization of IO@MS: IO@MS-NH_2. After CTAB washing via ammonium nitrate ion exchange, the IO@MS NPs were dispersed in 30 mL of EtOH and mixed overnight with 960 µL NH_3 and 4.5 mL of APTES. Then the particles were washed by centrifugation 3 times in EtOH and 3 times in water. The resulting IO@MS-NH_2 NPs were finally dispersed in 25 mL in Milli-Q water which correspond to a NPs concentration of 0.6 mg·mL^{-1}.

Dox loading. Dox loading into IO@MS-NH_2 NPs was performed by simple soaking of Dox with NPs in Milli-Q water. The soaking was achieved at a so called feed weight ratio (fwr) corresponding to the percentage of the ratio between the weight of Dox fed initially in the soaking media and the weight of NPs:

$$fwr\% = \frac{weight\ of\ Dox\ fed}{weight\ of\ NPs} \times 100$$

Thus after 24 h of mixing at a certain fwr, the Dox loaded IO@MS-NH_2 NPs were collected by centrifugation. The supernatants were measured by absorbance to calculate the amount of Dox loaded into the NPs. Furthermore 500 µL of each batch of IO@MS-NH_2 NPs dispersed in Milli-Q water were dry-freezed and then weighted to determine the initial concentration of IO@MS-NH_2 NPs. From these measurements, to evaluate the drug loading abilities of NPs, two essential entities were deduced: Drug Loading Content (DLC) and the Drug Loading Efficiency (DLE).

$$DLC\% = \frac{weight\ of\ Dox\ loaded}{weight\ of\ \text{NPs}} \times 100$$

$$DLE\% = \frac{weight\ of\ Dox\ loaded}{weight\ of\ Dox\ fed} \times 100$$

Fluorescent labeling of HSA. 531 µL of FITC in DMSO at 10 mg·mL^{-1} were mixed to 30 mL of HSA at 10 mg·mL^{-1} in 0.1 M sodium bicarbonate ($NaHCO_3$) buffer (pH 8.5). The mixture was stirred overnight and then dialyzed in MilliQ water to remove free FITC. The final volume was adjusted to 60 mL to have a HSA^{FITC} concentration of 5 mg·mL^{-1}.

Protocol of HSA coating. After the Dox loading, the HSA final coating was performed by using IBAM grafts. To functionalize the NPs surface with IBAM moieties, the sample was redispersed in 500 µL of DMF and 200 µL of Et_3N directly after Dox loading. Then a mixture of 270 µL of IBC in 2,5 mL of DMF was quickly added to the sample. A precipitate was formed immediately. These mixtures were stirred for 1 h and then 10 mL of HSA at 2 mg·mL^{-1} in Milli-Q water was added. After the addition of the HSA solution the precipitates were immediately dissolved. The solutions were stirred for additional 1h30 before being washed twice by centrifugation in water. Finally the resulting IO@MS-Dox-HSA NPs were dispersed in 3 mL of Milli-Q water (freeze-drying and subsequent weighing of the sample indicated a concentration of 0.4 mg·mL^{-1}).

The exact same protocols were carried out again on the previous silanized IO@MS NPs to produce the corresponding final NPs with HSA coating but without the loaded Dox. Two samples were executed: once using naturel HSA and a second with FITC-labelled HSA.

Protease degradation study. 200 µL of *Streptomyces griseus* proteases dissolved respectively at 25, 50 and 100 µg·mL^{-1} in PBS, were mixed with 200 µL of the previous IO@MS-HSA^{FITC} and IO@MS-Dox-HSA NPs. The mixture was incubated in water bath at 37°C and after a certain time

was centrifuged (7000 g / 10 min) in order to measure the fluorescence signal in the supernatant. After the fluorescent spectroscopy measurement, the supernatant was replaced in the mixture vial, the NPs were re-dispersed and put back at 37°C. This measure was repeated regularly over 20 hours.

Biological study.

Cell. Huh7-Luc, human hepatocarcinoma (ATCC®) were cultivated in Dulbecco's modified Eagle's medium supplemented with 10 % of decomplemented fetal bovine serum, penicillin streptomycine and non essential amino-acids.

Huh7-Luc multicellular tumor spheroid (MCTS) formation. Huh7-Luc MCTS were prepared using the hanging drop method. Previously a 96 well plate (Corning™ Costar™ Flat Bottom Cell Culture Plates, Fisher scientific, Ref 10792552) was prepared to be non-adhesive. 100 µl of poly(2-hydroxyethyl methacrylate) (poly-HEMA; sigma P3932-10G) 0.5 % (W/V) in 100% ethanol solution was added to each well. The plate was then incubated in a dry oven at 38 °C until complete evaporation of the solution. A Huh7-Luc cell suspension of 5300 cell/mL was prepared. 15 µL drops were put down the inside face of the coverslip of the 96 well plate. Each drop was centered on a well. 100 µL of PBS were added to each well and the coverslip replace on the plate. Having made so each drop of cell suspension hangs from the coverslip above a well of the 96 well plate. Plate was incubated for 3 days at 37°C and 5% CO_2. PBS was then discarded and replace by 200 µL of complete medium. Plate was centrifuged at 500 G for 30 sec in order to harvest the Huh7-Luc MCTS. At this stage we can expect one spheroid, about 100 µm diameter size, per well.

Confocal laser scan microscopy. Huh7-Luc MCTS were incubated for 24 h with IO@MS-Dox-HSA and IO@MS-HSA^{FITC} NPs. Half of the medium was then discarded from each well and replaced by PFA 8% in PBS. Huh7-Luc MCTS were then incubated for 1h at room temperature. Once fixation completed Huh7-Luc MCTS were first rinced in three consecutive bath of PBS and mounted on a glass slide in Antifade Mounting Medium (Vector laboratories, H-1000, Burlingame, CA). Manipulation of Huh7-Luc MCTS was performed with a 400 µm nylon loop under microscope. A glass coverslip of 12 mm diameter was used and sealed with nail varnish. Huh7-Luc MCTS observation was performed with a Zeiss LSM 710 confocal microscope and with a Plan Apochromat 40X objective. The following conditions were defined: FITC excitation = 488 nm (argon laser), emission = 496-540 nm; Doxorubicin excitation = 488 nm, emission = 540-600 nm. Images were analyzed with the software ImageJ.

Assessment of the antitumoral effect on Huh7-luc MCTS. The experiments were carried out in octuplicate in 96-well plate using the spheroids as previously described. The IO@MS-Dox-HSA NPs or IO@MS-HSA NPs were diluted in complete cell culture medium. Nanoparticles (11 µL) were then immediately added to each spheroid by further dilution into the cell culture medium (100 µL). Final concentrations were 50, 100, 250, 300 and 500 $\mu g \cdot mL^{-1}$. The spheroid growth was examined using a Nikon Eclipse TS100 microscope and a 10 X objective. Images were recorded at days 0, 2 and 6 with a Nikon Color CCD DS-Fi2 Camera and a DS-L3 camera controller. The area of each spheroid was measured using the NIH Image J software and reported in μm^2. The MCTS growth was calculated relative to the initial area (A0; day 0).

CHARACTERIZATION

Transmission Electron Microcopy (TEM) and Energy dispersive X-ray (EDX) analysis. NPs were deposited on Formvar-coated copper grids. TEM images and EDX spectra were aquired with a JEOL 2100 TEM instrument operating at 200 kV coupled with energy dispersive X-ray (EDX) spectroscopy. The size distribution of NPs was measured on more than 200 NPs.

Dynamic Light Scattering (DLS). The colloidal stability of NPs suspensions was assessed by measuring the particle size distribution using a nano-sizer MALVERN (nano ZS) zetasizer at a scattering angle of 173°.

Spectrofluorimetry. A SAFAS (Monaco) spectrophotometer was used to measure the amount of Dox loaded within the IO@MS NPs and to follow the HSA^{FITC} degradation under proteases action.. The Dox loading was estimated by analyzing the absorbance of the supernatant after soaking the free Dox with IO@MS for 24h and centrifugation. The HSA^{FITC} degradation by proteases was followed by analyzing the fluorescence of the supernatant after centrifugation at different time points.

ICP-AES. IO@MS NPs samples were digested in closed vessels with trace metals grade nitric acid (TraceSELECT, Fluka) at 200 °C. The amount of Fe and Si in mineralized samples was measured with ICP-AES (Varian 720ES). Emission intensities were measured at 259.940 nm for Fe and 252.851 nm for Si and compared to emission intensities of standards (0.05, 0.2, 1, 5 $mg \cdot L^{-1}$) prepared from a certified standard (1000 $mg \cdot L^{-1}$, CPI International)."

Relaxivity measurements. T_1 and T_2 relaxation times measurements of IO@MS NPs were performed with a Bruker Minipsec 60 (Karlsruhe,Germany) working at a Larmor frequency 60MHz (1.41 T) at 37°C. The longitudinal and transverse relaxivity values r_1 and r_2 were obtained according to the general equation of relaxivity $R=R_0+r[CA]$ where R is the relaxation rate (1/T) in the presence of the contrast agent (CA), R_0 the relaxation rate of the aquous medium in the absence of the CA and r the relaxivity value of the CA.

N_2 isotherm adsorption. Nitrogen adsorption isotherms were obtained on a Micrometrics ASAP 2420 Accelerated Surface Area and Porosimetry System at 77K under continuous adsorption conditions. Brunauer-Emmett-Teller (BET) method was used to determine the surface area as well as the total internal pore volume at P/P0 = 0.97. By applying the Barrett-Joyner-Halenda (BJH) method, the surface area, the cumulative pore volume, and the mesoporous pore size distribution (PSD) are determined during the adsorption and desorption steps.

Fourier Transform Infra-Red Spectroscopy (FTIR). The composition of the IO@MS NPs was verified by Fourier Transform Infra-Red Spectroscopy (FTIR) (Perkin Elmer instrument FTIR Spectrum Two).

RESULTS AND DISCUSSION

1. Synthesis and characterization of magnetic core@mesoporous silica shell NPs

First, we established a suitable protocol, inspired from the literature, to synthesize spherical, monodispersed in size, IO@MS NPs. The IO NPs were synthesised by thermal composition as described previously [29]. The resulting IO NPs, presented in **Figure 2.A-C** were monodispersed and spherical with a size of 9 ± 1 nm. Then, a MS shell was build at the surface of the IO NPs by CTAB surfactant mediated sol-gel approach according to a procedure adapted from Hyeon et al. [30]. CTAB surfactant removal was achieved by nitrate ammonium washing and followed by IR spectroscopy (**Figure S1**). TEM (**Figure 2.D and E**) and SEM (**Figure S2**) images, confirmed the formation of individual IO@MS core-shell NPs composed of a IO core of 9 nm in diameter surrounded by a porous silica shell of about 12 nm thickness. The monodispersity in size was assessed by measuring the size of at least 500 NPs from the TEM images. The resulting TEM size distribution graph, **Figure 2.F**, shows a narrow size distribution of the IO@MS NPs of 31 ± 3 nm.

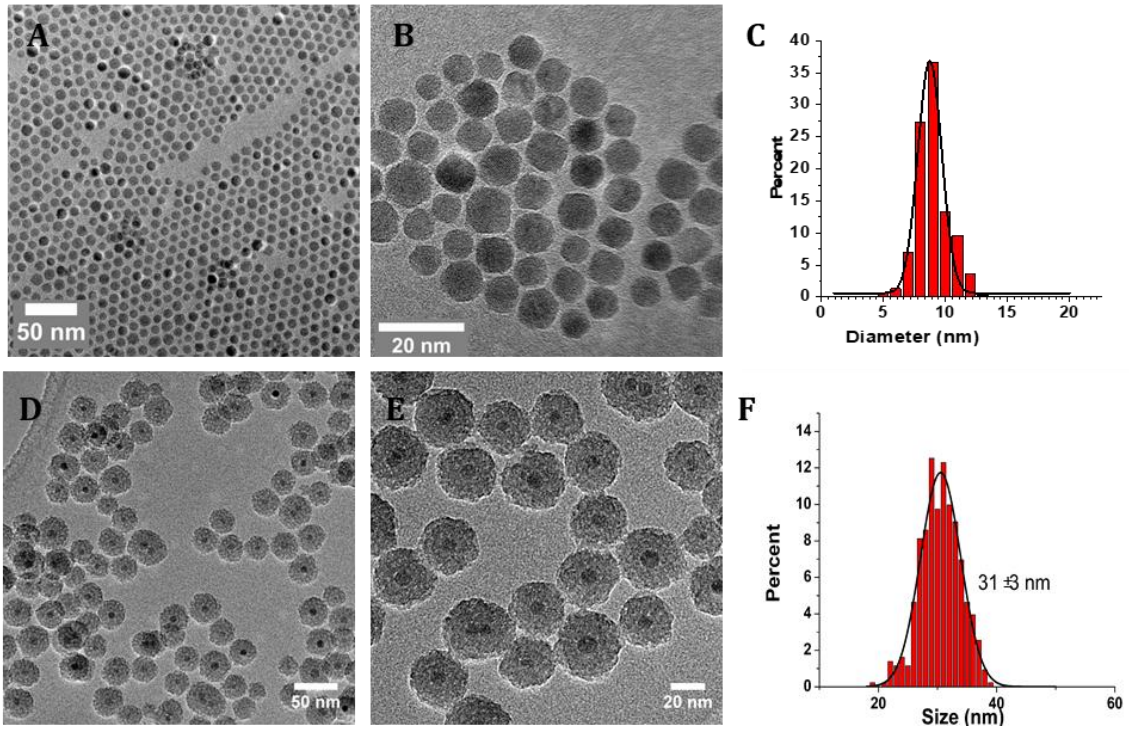

Figure 2. A) low and B) high magnification TEM images of IO NPs of 9 nm made by thermal decomposition. D) low and E) high TEM images of core-shell IO@MS NPs of 31 nm. C) and F) histograms of the TEM size distribution measured of both NPs on more than 500 particles.

FTIR spectra (**Figure 3.A**) proved the SiO_2 framework presence with characteristic peaks around 1098 and 804 cm^{-1} that correspond to ν_{as}(Si-O-Si) and ν_s(Si-O-Si). Regarding N_2 isotherm adsorption analysis, as depicted in **Figure 3.B-C**, the IO@MS NPs exhibited an expected type IV isotherm typical for mesoporous materials. The corresponding PSD curve, obtained through BJH calculations, shows pore sizes about 2.3 nm. As these core–shell NPs are very small in size, a large signal was also obtained for porosities higher than 10 nm resulting from the interparticle voids. A specific surface area of ~120 m^2/g was calculated. This value is a bit lower than the values found in the literature on similar systems, nevertheless, specific surface areas of 100 m^2/g are suitable for the loading and release of drug molecules.

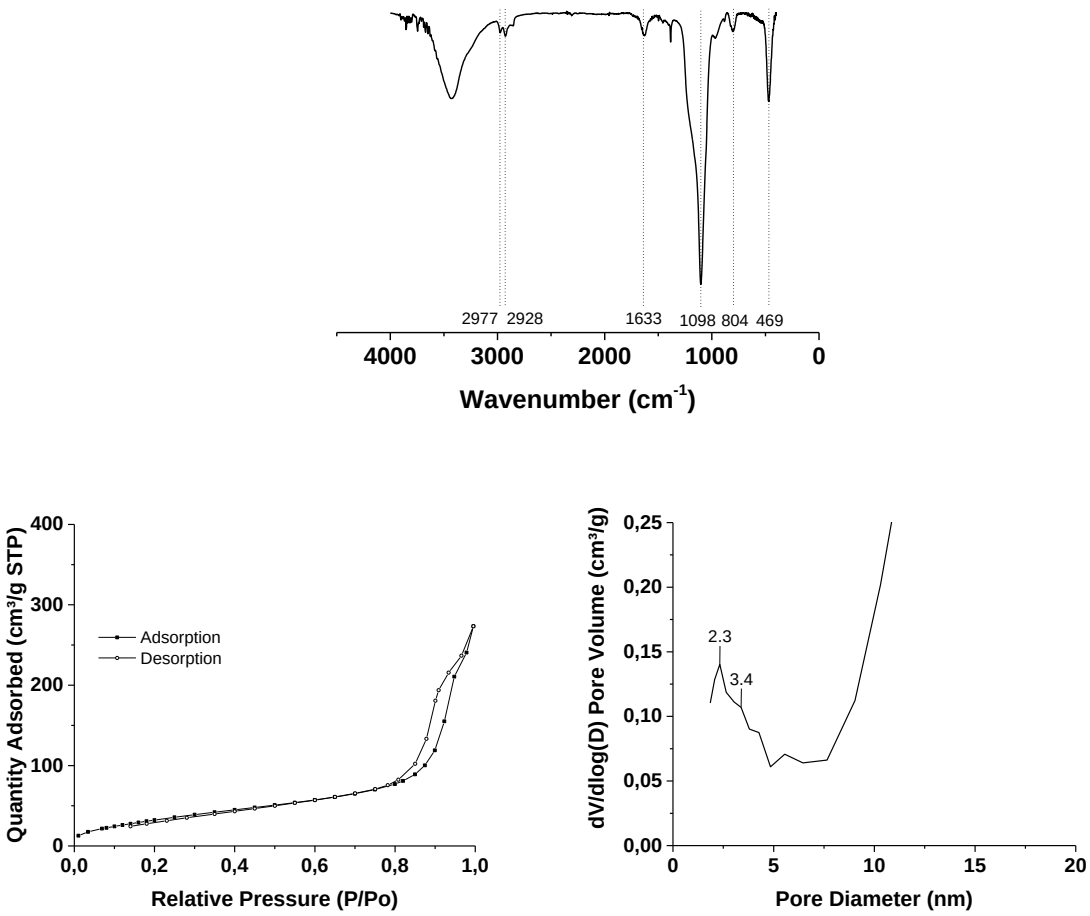

Figure 3. A) FTIR spectra of IO@MS NPs, B) N_2 adsorption-desorption isotherms and C) corresponding PSD curve for IO@MS NPs.

2. HSA coating on IO@MS NPs

In this section, with the aim to provide a biocompatible coating at the surface of the IO@MS, HSA was adsorbed at the surface of the IO@MS by using IBAM grafts as non-covalent binders. First, the surface of the IO@MS was modified with APTES. Then, the amine moieties reacted with *iso*butyrylchloride in DMF to form IBAM grafts. Finally, HSA was coated by simple adsorption in water. The TEM pictures, in **Figure 4. A and B**, of the protein coated NPs, IO@MS-HSA NPs, show that the IO@MS structure was not affected by this further sequential synthesis steps. Furthermore, we can distinguish that the porosities and the borders of the NPs appeared blurry, which could be ascribed to the HSA coating. In addition, the protein coating is also clearly visible between the NPs.

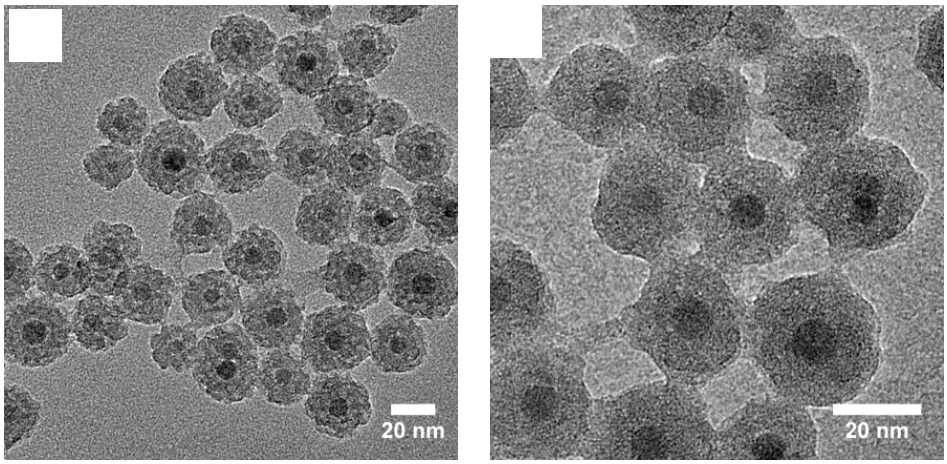

Figure 4. A) Low and B) high magnified TEM images of IO@MS NPs of 31 ± 3 nm coated with IBAM-HSA (denoted IO@MS-HSA)

TGA was performed to quantify the amount of the IBAM-HSA layer respectively to the inorganic core-shell. **Figure 6.** (black curve) shows the progressive calcination and evaporation of the organic layer from 25 to 600°C. Then the increase of mass observed is attributed to oxidation of the magnetic core. The first loss of mass of 5% was attributed to the water remaining in the system despite freeze-drying. Then IBAM-HSA layer was found to contribute to ca. 16.5% in mass which correspond to a coating of ca. 210 µg IBAM/HSA per mg of IO@MS core shell composite.

3. Evaluation of MRI contrast properties of IO@MS-HSA

Thanks to the superparamagnetic properties of the magnetite core, the IO@MS-HSA NPs may be used as T_2 contrast agents. This property was assessed by proton NMR relaxometry at 37 °C and 1.41 T (60 MHz). These NPs were dispersed in PBS buffer in order to avoid pH variation between measurements. Longitudinal (T_1) and transverse (T_2) relaxation times of protons were

measured at various Fe concentrations, [Fe]. The highest [Fe] was measured initially by ICP-AES, and the lower [Fe] were obtained by dilution. As expected, the resulting relaxivity curves $1/T_1$ and $1/T_2$ in function of [Fe], presented in **Figure 5.A and B** respectively, showed linear behaviors. The slopes of the linear fit of these curves gave the r_1 and r_2 values.

The specific relaxivity values of IO@MS-HSA were of r_1= 0.15 $mM^{-1}s^{-1}$ and r_2= 70 $mM^{-1}s^{-1}$. In a previous study on the same kind of IO NPs coated with TPEDTA siloxane (free silica) instead of MS-HSA shell, we obtained a r_1 of 13.9 $mM^{-1}s^{-1}$ and a r_2 of 88.6 $mM^{-1}s^{-1}$.[32] Our present study here on IO@MS-HSA NPs showed that the MS-HSA coating on the IO NPs did not modify importantly the r_2 value as compared to IO@TPEDTA but strongly decreased the r_1 leading to a higher r_2/r_1 ratio. This low r_1 value could be explained by a limited water accessibility to the magnetic core due to the MS-HSA coating. Furthermore, the r_2 value of IO@MS-HSA NPs was in the same range than r_2 of commercially used IO, 120 $mM^{-1}s^{-1}$ for Feridex, 186 $mM^{-1}s^{-1}$ for Resovist and 65 $mM^{-1}s^{-1}$ for Combidex.[33] Thus these results place our system as potential candidate for T_2 contrast agents.

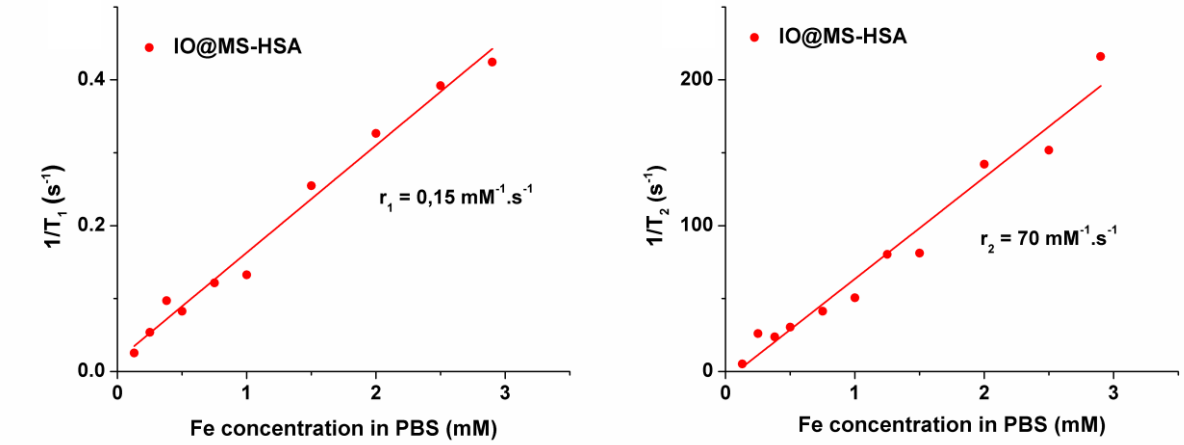

Figure 5. T_1 and T_2 relaxometry curves of IO@MS-HSA of 30 nm in diameters (A and B respectively).

4. Dox encapsulation in IO@MS -HSA NPs

Our IO@MS-HSA NPs are promising T_2 contrast agent candidates. However, in order to make them good candidates as theranostics agents, their cargo capacities for drug delivery had to be tested. Hence, in this part, the IO@MS-HSA sample was loaded with Dox before the HSA coating step. To be sure to reach the maximum DLC possible, a high fwr of 170% was choosed. The DLC and DLE values measured by indirect method of the supernatant absorbance analysis at this fwr were respectively of 34w% and 20w% (see calibration curve in **Figure S3**). In the final formulation IO@MS-Dox-HSA, it was important to determine if some Dox was released during

the subsequent synthesis steps (IBAM modification and HSA coating). Thus comparative TGA analyses between Dox-loaded IO@MS-Dox-HSA and non-loaded IO@MS-HSA NPs were also run (**Figure 6)**. Free Dox and HSA TGA analyses (**Figure S4**) show similar calcination signals allowing predicting similar behaviors on the IO@MS composites. According to the TGA curves of IO@MS-HSA and the IO@MS-Dox-HSA NPs, 58 % of IO@MS-Dox-HSA sample corresponded to the inorganic IO@MS NPs whereas 5 % came from the remaining water, 16,5 % from the IBAM-HSA coating and 20 % from the Dox loading. Thus, this corresponds to a DLC of 34 % of Dox loaded into raw IO@MS NPs. This result is matching the DLC value obtained with the supernatant analysis after Dox impregnation suggesting that a negligeable amount of Dox was released from the NPs during the synthesis steps for the protein coating.

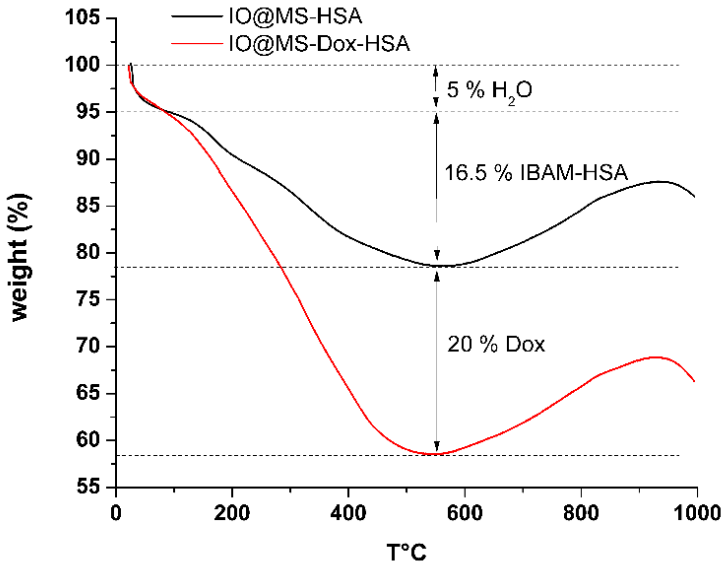

Figure 6. TGA curves of IO@MS-HSA and IO@MS-Dox-HSA NPs

The colloidal stability of IO@MS-Dox-HSA NPs was assessed in water. **Figure 7.A** presents the DLS measurement in volume of IO@MS and IO@MS-Dox-HSA NPs in water (**Figure S5** shows the DLS measurements in intensity and number). These results showed a similar behavior for both raw IO@MS and final IO@MS-Dox-HSA NPs meaning that the modification of the IO@MS with Dox loading and IBAM-HSA coating did not change the colloidal stability of the system. No NPs aggregation can be observed. Hence, a major contribution with hydrodynamic sizes of ca. 58 nm and second minor contribution at ca. 200 nm were observed.

The Zeta-potential measurements, in **Figure 7. B**, show that IO@MS-NH_2 NPs have an IEP around 7.7. Therefore, they were positively charged before the Dox loading, with a Zeta potential over +20 mV, in the pH range of Milli-Q water, pH 6-7. As the Dox hydrochloride salt is well positively charged in Milli-Q water we can conclude through this Zeta potential measurements

that the interactions between the amino-modified silica surface and the Dox were not of electrostatic nature. After the Dox loading and HSA coating, the IEP of these particles decrease to 6. IO@MS-Dox-HSA NPs are then slightly negatively charged, with a Zeta potential between 0 and -20 mV, in the Milli-Q water pH range. This should have led to poor colloidal stability according to such low ZP values. However, according to the DLS results for this compound and the excellent colloidal stability observed (see photograph of a suspension in **Figure S6)**, the NPs were found to have a great colloidal dispersion. This good colloidal stability can be more attributed to steric effects of the HSA layer than to repulsive forces with less contribution of electrostatic interactions.

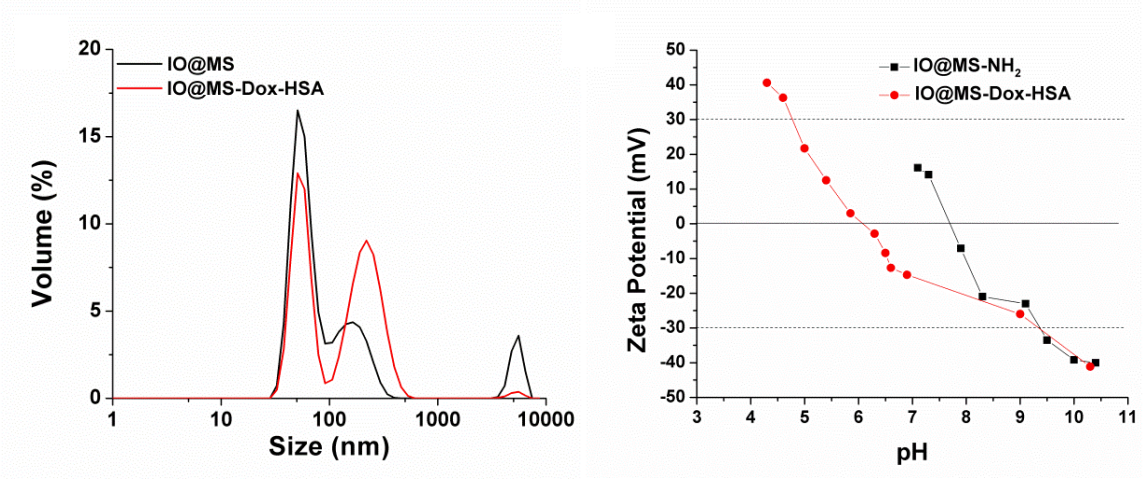

Figure 7. A) DLS measurement of IO@MS and IO@MS-Dox-HSA NPs and B) Zeta potentials of IO@MS-NH_2 and IO@MS-Dox-HSA NPs.

5. Dox release through degradation of the protein shell.

To test the bio-responsiveness of the protein nanocoating for controlled drug delivery, IO@MS-Dox-HSA NPs were incubated with protease solutions at various concentrations. The objective here was to investigate the Dox release after HSA shell enzymatic degradation.

For this purpose, a first sample without Dox but with FITC-labelled HSA (called IO@MS-HSA^{FITC}) and a second sample with Dox but with non-labelled HSA (called IO@MS-Dox-HSA) were prepared. The NPs were incubated at 37 °C in PBS at pH 7.4 with various proteases concentrations: 1000, 500 and 100 $\mu g \cdot mL^{-1}$. At predetermined time intervals, the mixtures were centrifuged and the supernatants were analyzed by fluorescence spectroscopy with λ_{exc}= 488 nm and λ_{em}=520 nm for IO@MS-HSA^{FITC} and with λ_{exc}= 488 nm and λ_{em}=595 nm for the Dox-loaded sample. **Figure 8** shows the profiles of HSA degradation (**8.A**) and Dox release (**8.B**) of the

samples. The increase of fluorescence intensity in IO@MS-HSA^{FITC} in contact with proteases confirmed that HSA^{FITC} was progressively degraded in the presence of proteases. Degradation rate is driven by enzyme concentration. No fluorescence was recorded in control sample, in the absence of protease. It confirms that the HSA shell is stable by the time course of the experiment and that the proteases are mandatory for the shell degradation. However, no significant Dox release was recorded in presence of protease.

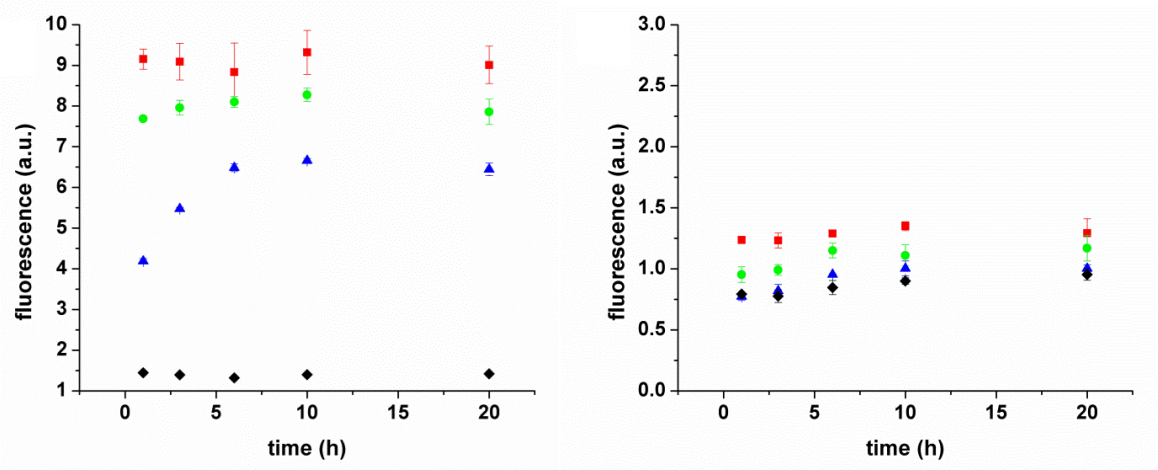

Figure 8. Kinetic profiles under various proteases concentration ((■) 1000 µg/mL, (●) 500 µg/mL (▲) 500 µg/mL, (◆) 0 µg/mL) at 37 °C in PBS at pH 7.4 of A) HSA^{FITC} degradation from IO@MS-HSA^{FITC} sample, B) Dox release from IO@MS-Dox-HSA sample.

To understand this effect, we thus acquired fluorescence emission spectra of DOX in water in three systems: free Dox in solution (Fig. **S7.A**), IO@MS-Dox (after APTS and before IBAM modifications) (Fig. **S7.B**) and IO@MS-Dox-HSA (after IBAM-HSA modification, Fig **S7.C**). Analysis of the spectra indicates that the spectral characteristics of Dox are very similar for free Dox and IO@MS-Dox. Indeed Dox presents two fluorescence emission maxima at *ca.* 570 nm and 599 nm. This indicates that Dox does not suffer any change of chemical structure after impregnation in the core–shell system. Regarding the spectral characteristics of IO@MS-Dox-HSA, some changes can be observed especially in the second band of emission which was reduced. This result suggests that a non-negligible part of the Dox molecules was degraded during the process IBAM-HSA. Thus, Dox molecules impregnated at the outer surface of the NPs are probably altered by the IBAM grafting procedure while the Dox molecules impregnated in depth in the pores are more likely not altered. At least, to elucidate the reactant responsible for the Dox alteration, we acquired spectrofluorometric spectra in the reaction media in DMF of Dox, Dox with Et_3N and Dox with Et_3N + *iso*butyrylchloride (IBC). Data in figure **S8** show that while Dox spectra are very similar between Dox and Dox+Et_3N, the absence of spectrum for Dox+Et_3N+IBC demonstrated the clear degradation of Dox under these conditions. These data

show that the acidity generated by IBC is probably the main responsible agent for Dox degradation.

Finally, the preservation of both the red color of our suspension (**Fig. S6**) and the two emission peaks, strongly indicates that the Dox degradation is only partial when loaded into IO@MS NPs, while it is total for free Dox in solution. Hence the nano-confinement within the pores, like a "ship in a bottle", may ensure retention of Dox structure and its activity however it may also explain why the Dox hardly release upon protease action despite effective HSA shell degradation. Thus, bench conditions where only one biochemical stimulus is applied (protease at 1mg·mL^{-1} maximum) is not sophisticated enough to allow an effective Dox release. . With the aim to investigate if Dox release would occur in a more complex media endowed with various biochemical stimuli, we directly assessed, in the next paragraphs, our IO@MS-Dox-HSA NPs on 3D cellular models (spheroids).

6. Evaluation of IO@MS-HSA NPs diffusion and Dox release in Huh7-Luc MCTS model.

One of the major drawbacks concerning the use of NPs in medicine is their poor diffusion in tissue. Indeed, depending on their size but as well as the type of tissue, the diffusion can be rather limited. Even if two-dimensional (2D) cell monolayers have been conventionally used by the scientific community to evaluate drug efficacy, NPs cytotoxicity and their internalization, they poorly represent the complex tumor 3D microenvironment. Indeed, cells grown in 2D lack the extracellular matrix (ECM), as well as cell-cell contact and cell-matrix interactions. Thus, The developpement of 3D culture models have emerged as an additional *in vitro* step study to assist drug product development and tend to reduce the requirement for unnecessary animal studies [34–41]]. However, based on the so-called enhanced permeation and retention effect described for some tumors, NPs could help to deliver locally the chemotherapeutic agent and avoid side effects as it would only diffuse in the tumor. In our strategy we aim to deliver Dox in a controlled manner: by the protease degradation of the HSA coating. Dox is a small molecule able to diffuse freely through cell plasma membrane. Thanks to its inner fluorescence, it is easily detectable by microscopy. We thus tested the internalization of the NPs and their diffusion in a Huh7-Luc MCTS model and follow the subsequent diffusion of Dox loaded in the nanoparticles. To do so, Huh7-Luc MCTS were incubated 24h with IO@MS-HSA^{FITC} and IO@MS-Dox-HSA samples.

First, internalization of the IO@MS-HSA^{FITC} NPs into the spheroids was imaged by confocal microscopy at two Fe concentrations (0.4 and 0.8 µg Fe·mL^{-1}). The resulting images are presented in **Figure 9.** At 0.4 µg Fe·.mL^{-1}, IO@MS-HSA^{FITC} NPs was clearly visible only in the top and bottom images. At 0.8 µg Fe·mL^{-1}, images of the core region of the spheroids showed clearly that the internalization of the IO@MS-HSA^{FITC} NPs occurred at the spheroid border with a

penetration depth of about 10 to 20 μm, which is the size of a cell. Such results are in accordance with previous work showing that, for gold NPs with a diameter above 5 nm, their diffusion in such MCTS is abolished. [42,43]

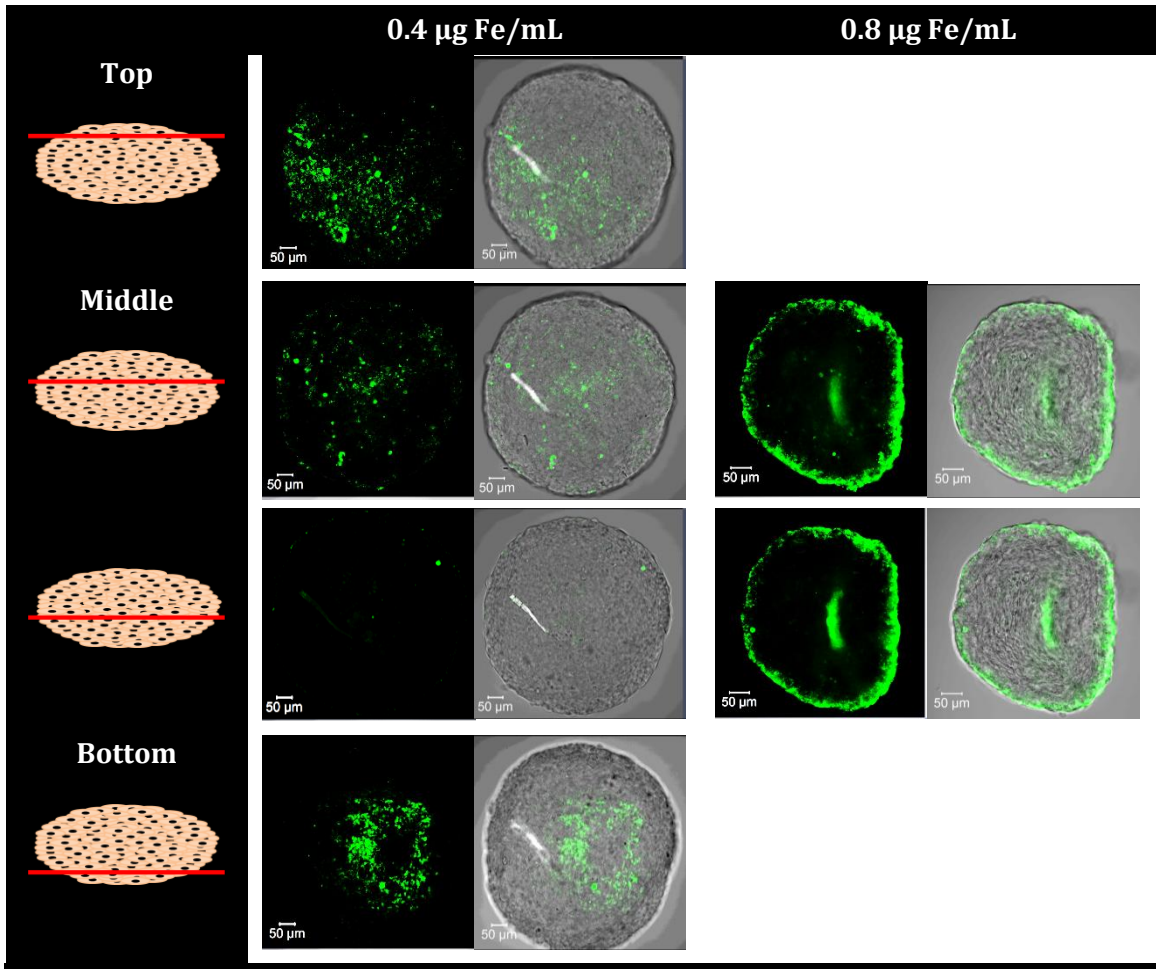

Figure 9. CLSM imaging of Huh7-Luc MCTS after 24h incubation with IO@MS-HSA^{FITC} NPs at 0.4 and 0.8 µg Fe·mL^{-1}. Images show the entire spheroid analysis (Z-stack). The magnification used in CLSM is x 40.

We then assessed the diffusion of Dox from the IO@MS-Dox-HSA NPs internalized in Huh7-Luc MCTS. First, Z-stack images were performed on spheroids incubated for 24 h at various concentrations of free Dox (0, 0.01 and 3 $\mu g \cdot mL^{-1}$) to evaluate Dox behavior in our model. As pictured on the images summarized in **Figure S9**, Dox accumulated after 24 h of incubation into the nuclei of the cells. Fluorescence intensity recorded, keeping the same setting parameters, are correlated with the various Dox concentrations tested. For 3 $\mu g \cdot mL^{-1}$ of Dox, the laser intensity used in the imaging parameters was too high and led to saturated images. Then, Dox localisation into MCTS was assessed after internalization of IO@MS-Dox-HSA NPs by Z-stack analyses with the same setting as previously. IO@MS-Dox-HSA NPS were studied at Fe concentrations of 0.8 and 0.4 $\mu g \cdot mL^{-1}$**(Figure 10).** As seen in **Figure 10**, after 24h incubation Dox seems to be disseminated into the entire MCTS. It proves that once the IO@MS-Dox-HSA NPs are internalised in the border cells they underwent protease degradation. Surprisingly no Dox was found accumulated at the border with the same images we get with the FITC labeled particles. It could be interpreted as a complete release of the Dox in the incubation time.

Finally, we can state that even if the NPs were stayed only at the periphery of the spheroids, they could ensure the local release of Dox that can then diffuse into the entire 3D model. Such behavior could sign the lag between the particle internalization and Dox release as it is triggered by HSA digestion probably by proteases found in endo-lysosome. Such 3D culture system is a model of early tumorogenesis process. So these results help to envision how such particles could work on *in-vivo* models.

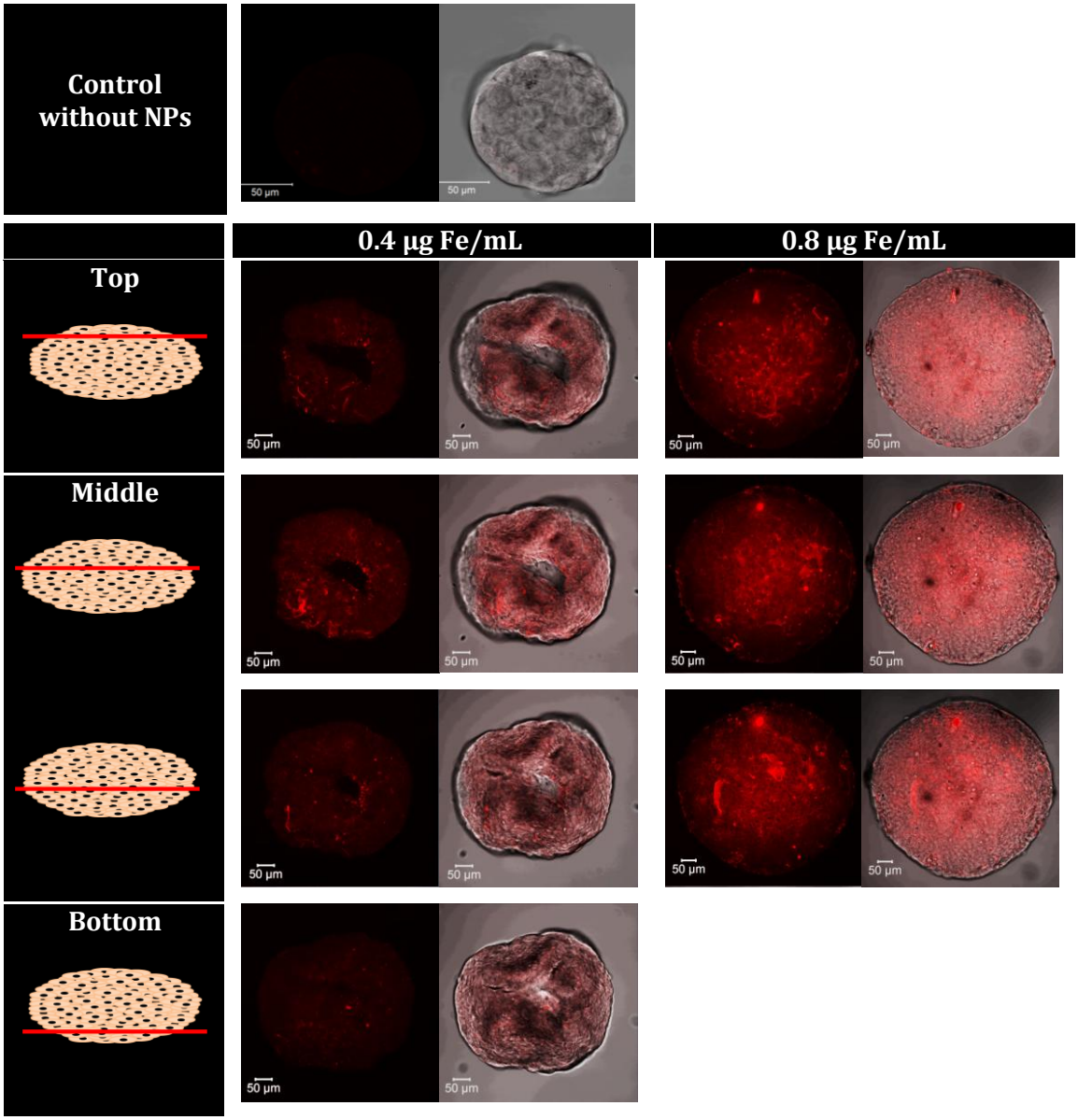

Figure 10. High resolution CLSM imaging of Huh-7 MCTS after 24h incubation with IO@MS-Dox-HSA NPs at 0.4 and 0.8 µg Fe·mL^{-1}. The magnification used in CLSM is x 40.

7. Assessment of the antitumoral effect on Huh7-luc MCTS.

To assess the cell cytotoxicity and the antitumoral effect of the core-shell nanoparticles, we used Huh7-Luc MCTS growth monitoring. Huh7-Luc MCTS were cultivated during 6 days in presence of IO@MS-Dox-HSA NPs or IO@MS-HSA NPs of various concentrations. At day 2 and 6 the Huh-7 Luc MCTS area was measured and compared to area of the control Huh7-Luc MCTS that have grown without particles. As shown in the figure below, for the samples up to 100 µg·mL^{-1}no cytotoxicity is recorded with a growth of the spheroids in presence of NPs comparable to the control. From 250 µg·mL^{-1} up to 500 µg·mL^{-1} , the NPs show some cytotoxicity that is correlated

to the concentration. However, we can clearly note a difference in the Huh7-Luc growth between IO@MS-Dox-HSA NPs or IO@MS-HSA NPs. Indeed, at 250 and 300 µg·mL^{-1}, IO@MS-Dox-HSA NPs show more growth inhibition than IO@MS-HSA NPs (respectively 54 % vs 32 % inhibition for 250 µg·mL^{-1} and 75% vs 61 % inhibition for 300 µg·mL^{-1} at D6). This difference could be attributed to the release of Dox into the spheroids by the time. Nevertheless, this effect is abolished at the highest concentration of 500 µg·mL^{-1} showing a severe cell cytotoxic effect for both cases (86 % growth inhibition at D6). Altogether those results show that we do have an active release of Dox by the time once the NPs have been internalized in the Huh7-luc spheroids, but the inherent cytotoxicity impedes the use of a higher concentration that could have a more potent antitumor effect.

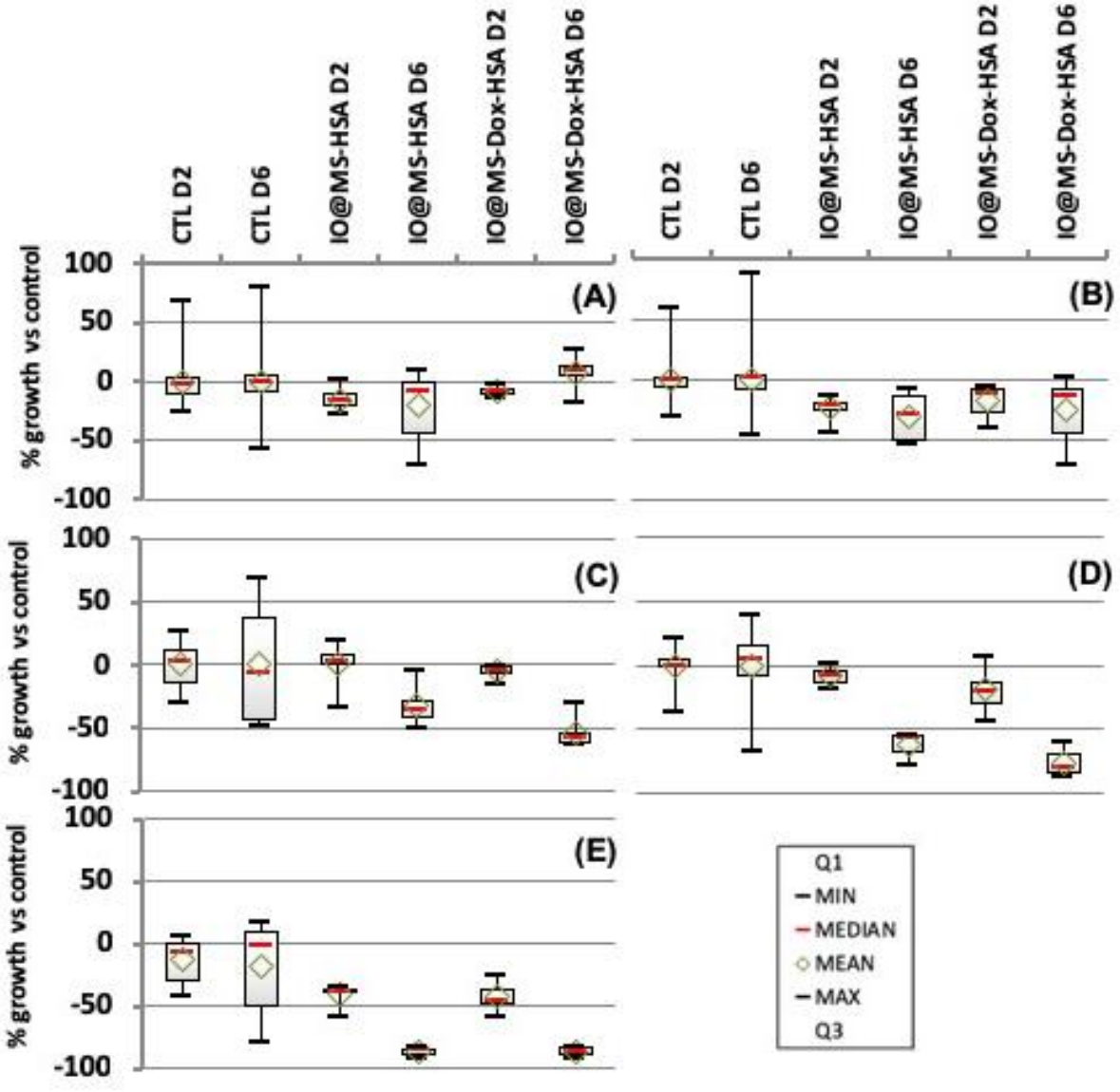

Figure 11. Evolution of % spheroid growth vs control of Huh7-luc MCTS at days 0, 2 and 6 carried out in octuplicate after incubation of IO@MS-Dox-HSA NPs or IO@MS-HSA NPs. NPs concentrations are 50 (A), 100 (B), 250 (C), 300(D) and 500 $\mu g \cdot mL^{-1}$. (E). The MCTS growth was calculated relative to the initial area (A0; day 0).

Finally, in this biological study, we confirmed that in a cell media like a spheroid, the various and complex biochemical stimuli secreted by the cells were able to unstick the Dox confined and ensure its release in the spheroids as observed by confocal microscopy. Moreover, the cytotoxic study above indicates a cytotoxic effect of the Dox. These results are in agreement with study that we published recently, where we used the same chemical strategy to immobilize Dox in HSA capsules (DOX loading between APTS and IBAM in HSA wall)[44]. The Dox-loaded HSA nanocapsules were formed after sacrificial dissolution of the silica template. Here we also observed the same behavior than in the present work: no Doxorubicin release was observed after HSA capsule incubation with protease while a strong cytotoxicity was observed on spheroids as compared to the non-loaded HSA capsules.

Overall, the results addressed in this work, suggest that in such core shell constructs, an important part of Dox keeps its structural properties, is able to diffuse into the spheroid, and, acts as cytotoxic agents by killing human cancer cells.

Conclusion

In this work, the design and full characterization of new hybrid spherical monodisperse IO@MS nanocomposites covered with IBAM-HSA coating, and denoted IO@MS-HSA NPs was achieved. These nanocomposites were analyzed by proton relaxometry, and the HSA coated IO@MS NPs were shown to display significantly high T_2 contrast properties, with a transverse relaxivity r_2 of 70 $Mm.s^{-1}$. Then, impregnation of Dox achieved on IO@MS NPs modified with APTS in water, led to a very high DLC value in the range of 35% which was also confirmed in the final IO@MS-Dox-HSA. Furthermore, regarding the drug release, we found out that, after Dox loading and capping by a tight HSA shell, an efficient HSA shell degradation was observed under enzymatic action. Dox release was objectivized in Huh7-Luc MCTS. Indeed, after only 24h incubation, IO@MS-Dox-HSA internalized into the border cell of the spheroid release their Dox that can freely diffuse into the tissue and inhibit the spheroid growth. This new hybrid protein coated magnetic core-MS shell could thus be envisionned as a new type of theranostic agents displaying in the same formulation abilities for antitumoral drug release and T_2 contrast for MRI diagnosis.

Supporting information. S1. FTIR spectra of IO@MS NPs before CTAB washing, and after nitrate ammonium washings, S2. SEM image of the IO@MS NPs, S3. TGA of free Dox and free

HSA, S4. DLS measurement of IO@MS and IO@MS-Dox-HSA in A) intensity an B) number. S5. Photograph of IO@MS@Dox-HSA NPs highlighting their colloidal stability, S6. CLSM images of free Dox penetration into spheroids

Acknowledgements.

C. Ulhaq and D. Ihiawakrim are acknowledged for assistance with TEM microscope. D. Bégin and K. Parkhomenko are acknowledged for helpful discussion. A. Boos and P. Ronot are acknowledged for ICP-AES experiments. D.M. thanks the University of Strasbourg for financial support from IDEX-Attractivité framework. S. B.C, D. M. and F.M. thank ARC (Association de recherche contre le Cancer), IHU (Institut Hospitalo-Universitaire) de Strasbourg for financial support under the TheraHCC framework and Alsace contre le Cancer for financial support under the Venacoco project. The Institut National du Cancer (INCa) is also acknowledged for the financial support (project PRTK14,THERAMAG 2014-225).

REFERENCES

[1] Janib S M, Moses A S and MacKay J A 2010 Imaging and drug delivery using theranostic nanoparticles *Adv. Drug Deliv. Rev.* **62** 1052–1063

[2] Lammers T, Aime S, Hennink W E, Storm G and Kiessling F 2011 Theranostic nanomedicine *Acc. Chem. Res.* **44** 1029–1038

[3] Lee D-E, Koo H, Sun I-C, Ryu J H, Kim K and Kwon I C 2012 Multifunctional nanoparticles for multimodal imaging and theragnosis *Chem. Soc. Rev.* **41** 2656–2672

[4] Mahmoudi M, Sant S, Wang B, Laurent S and Sen T 2011 Superparamagnetic iron oxide nanoparticles (SPIONs): development, surface modification and applications in chemotherapy *Adv. Drug Deliv. Rev.* **63** 24–46

[5] Kievit F M and Zhang M 2011 Surface engineering of iron oxide nanoparticles for targeted cancer therapy *Acc. Chem. Res.* **44** 853–862

[6] Blanco-Andujar C, Walter A, Cotin G, Bordeianu C, Mertz D, Felder-Flesch D and Begin-Colin S 2016 Design of iron oxide-based nanoparticles for MRI and magnetic hyperthermia *Nanomed.* **11** 1889–1910

[7] Walter A, Billotey C, Garofalo A, Ulhaq-Bouillet C, Lefèvre C, Taleb J, Laurent S, Vander Elst L, Muller R N and Lartigue L 2014 Mastering the shape and composition of dendronized iron oxide nanoparticles to tailor magnetic resonance imaging and hyperthermia *Chem. Mater.* **26** 5252–5264

[8] Stanicki D, Vander Elst L, Muller R N, Laurent S, Felder-Flesch D, Mertz D, Parat A, Begin-Colin S, Cotin G, Greneche J-M, Ersen O, Pichon B, Socoliuc V, Kuncser V, Turcu R, Vekas L, Foster P and Bartha R 2018 Chapter 4 Iron-oxide Nanoparticle-based Contrast Agents

Contrast Agents for MRI: Experimental Methods (The Royal Society of Chemistry) pp 318–447

[9] Knežević N Ž, Ruiz-Hernández E, Hennink W E and Vallet-Regí M 2013 Magnetic mesoporous silica-based core/shell nanoparticles for biomedical applications *Rsc Adv.* **3** 9584–9593

[10] Hervault A and Thanh N T K 2014 Magnetic nanoparticle-based therapeutic agents for thermo-chemotherapy treatment of cancer *Nanoscale* **6** 11553–11573

[11] Oliveira H, Pérez-Andrés E, Thevenot J, Sandre O, Berra E and Lecommandoux S 2013 Magnetic field triggered drug release from polymersomes for cancer therapeutics *J. Controlled Release* **169** 165–170

[12] Mertz D, Sandre O and Bégin-Colin S 2017 Drug releasing nanoplatforms activated by alternating magnetic fields *Biochim. Biophys. Acta BBA - Gen. Subj.* **1861** 1617–41

[13] Kralj S, Potrc T, Kocbek P, Marchesan S and Makovec D 2017 Design and fabrication of magnetically responsive nanocarriers for drug delivery *Curr. Med. Chem.* **24** 454–469

[14] Hervault A, Dunn A E, Lim M, Boyer C, Mott D, Maenosono S and Thanh N T 2016 Doxorubicin loaded dual pH-and thermo-responsive magnetic nanocarrier for combined magnetic hyperthermia and targeted controlled drug delivery applications *Nanoscale* **8** 12152–12161

[15] Nigam S, Chandra S, Newgreen D F, Bahadur D and Chen Q 2014 Poly (ethylene glycol)-modified PAMAM-Fe3O4-doxorubicin triads with the potential for improved therapeutic efficacy: generation-dependent increased drug loading and retention at neutral pH and increased release at acidic pH *Langmuir* **30** 1004–1011

[16] Gaihre B, Khil M S, Lee D R and Kim H Y 2009 Gelatin-coated magnetic iron oxide nanoparticles as carrier system: drug loading and in vitro drug release study *Int. J. Pharm.* **365** 180–189

[17] Lee J E, Lee D J, Lee N, Kim B H, Choi S H and Hyeon T 2011 Multifunctional mesoporous silica nanocomposite nanoparticles for pH controlled drug release and dual modal imaging *J. Mater. Chem.* **21** 16869–16872

[18] N'Guyen T T T, Duong H T T, Basuki J, Montembault V, Pascual S, Guibert C, Fresnais J, Boyer C, Whittaker M R, Davis T P and Fontaine L 2013 Functional Iron Oxide Magnetic Nanoparticles with Hyperthermia-Induced Drug Release Ability by Using a Combination of Orthogonal Click Reactions *Angew. Chem. Int. Ed.* **52** 14152–6

[19] Yuan L, Tang Q, Yang D, Zhang J Z, Zhang F and Hu J 2011 Preparation of pH-responsive mesoporous silica nanoparticles and their application in controlled drug delivery *J. Phys. Chem. C* **115** 9926–9932

[20] Shen J, He Q, Gao Y, Shi J and Li Y 2011 Mesoporous silica nanoparticles loading doxorubicin reverse multidrug resistance: performance and mechanism *Nanoscale* **3** 4314–4322

[21] Liu J, Detrembleur C, De Pauw-Gillet M-C, Mornet S, Vander Elst L, Laurent S, Jérôme C and Duguet E 2014 Heat-triggered drug release systems based on mesoporous silica nanoparticles filled with a maghemite core and phase-change molecules as gatekeepers *J. Mater. Chem. B* **2** 59–70

[22] Andreasen S Ø, Fejerskov B and Zelikin A N 2014 Biocatalytic polymer thin films: optimization of the multilayered architecture towards in situ synthesis of anti-proliferative drugs *Nanoscale* **6** 4131–4140

[23] Vogt C, Mertz D, Benmlih K, Hemmerlé J, Voegel J-C, Schaaf P and Lavalle P 2012 Layer-by-Layer Enzymatic Platform for Stretched-Induced Reactive Release *ACS Macro Lett.* **1** 797–801

[24] Barthes J, Mertz D, Bach C, Metz-Boutigue M-H, Senger B, Voegel J-C, Schaaf P and Lavalle P 2012 Stretch-induced biodegradation of polyelectrolyte multilayer films for drug release *Langmuir* **28** 13550–13554

[25] Mertz D, Tan P, Wang Y, Goh T K, Blencowe A and Caruso F 2011 Bromoisobutyramide as an Intermolecular Surface Binder for the Preparation of Free-standing Biopolymer Assemblies *Adv. Mater.* **23** 5668–73

[26] Mertz D, Cui J, Yan Y, Devlin G, Chaubaroux C, Dochter A, Alles R, Lavalle P, Voegel J C and Blencowe A 2012 Protein capsules assembled via isobutyramide grafts: sequential growth, biofunctionalization, and cellular uptake *ACS Nano* **6** 7584–7594

[27] Mertz D, Wu H, Wong J S, Cui J, Tan P, Alles R and Caruso F 2012 Ultrathin, bioresponsive and drug-functionalized protein capsules *J. Mater. Chem.* **22** 21434–21442

[28] Mertz D, Affolter-Zbaraszczuk C, Barthès J, Cui J, Caruso F, Baumert T F, Voegel J-C, Ogier J and Meyer F 2014 Templated assembly of albumin-based nanoparticles for simultaneous gene silencing and magnetic resonance imaging *Nanoscale* **6** 11676–11680

[29] Baaziz W, Pichon B P, Fleutot S, Liu Y, Lefevre C, Greneche J-M, Toumi M, Mhiri T and Begin-Colin S 2014 Magnetic iron oxide nanoparticles: reproducible tuning of the size and nanosized-dependent composition, defects, and spin canting *J. Phys. Chem. C* **118** 3795–3810

[30] Kim J, Kim H S, Lee N, Kim T, Kim H, Yu T, Song I C, Moon W K and Hyeon T 2008 Multifunctional uniform nanoparticles composed of a magnetite nanocrystal core and a mesoporous silica shell for magnetic resonance and fluorescence imaging and for drug delivery *Angew. Chem. Int. Ed.* **47** 8438–8441

[31] Ye F, Laurent S, Fornara A, Astolfi L, Qin J, Roch A, Martini A, Toprak M S, Muller R N and Muhammed M 2012 Uniform mesoporous silica coated iron oxide nanoparticles as a highly efficient, nontoxic MRI T2 contrast agent with tunable proton relaxivities *Contrast Media Mol. Imaging* **7** 460–468

[32] Wang X-Y, Mertz D, Blanco-Andujar C, Bora A, Ménard M, Meyer F, Giraudeau C and Bégin-Colin S 2016 Optimizing the silanization of thermally-decomposed iron oxide nanoparticles for efficient aqueous phase transfer and MRI applications *RSC Adv.* **6** 93784–93793

[33] Na H B, Song I C and Hyeon T 2009 Inorganic nanoparticles for MRI contrast agents *Adv. Mater.* **21** 2133–2148

[34] Hamilton G 1998 Multicellular spheroids as an in vitro tumor model *Cancer Lett.* **131** 29–34

[35] Kunz-Schughart L A 1999 Multicellular tumor spheroids: intermediates between monolayer culture and in vivo tumor *Cell Biol. Int.* **23** 157–61

[36] Lin R-Z and Chang H-Y 2008 Recent advances in three-dimensional multicellular spheroid culture for biomedical research *Biotechnol. J.* **3** 1172–84

[37] Hirschhaeuser F, Menne H, Dittfeld C, West J, Mueller-Klieser W and Kunz-Schughart L A 2010 Multicellular tumor spheroids: An underestimated tool is catching up again *J. Biotechnol.* **148** 3–15

[38] Hutmacher D W 2010 Biomaterials offer cancer research the third dimension *Nat. Mater.* **9** 90–3

[39] Mehta G, Hsiao A Y, Ingram M, Luker G D and Takayama S 2012 Opportunities and challenges for use of tumor spheroids as models to test drug delivery and efficacy *J. Controlled Release* **164** 192–204

[40] Fitzgerald K A, Malhotra M, Curtin C M, O' Brien F J and O' Driscoll C M 2015 Life in 3D is never flat: 3D models to optimise drug delivery *J. Controlled Release* **215** 39–54

[41] Asghar W, El Assal R, Shafiee H, Pitteri S, Paulmurugan R and Demirci U 2015 Engineering cancer microenvironments for in vitro 3-D tumor models *Mater. Today* **18** 539–53

[42] Huang K, Ma H, Liu J, Huo S, Kumar A, Wei T, Zhang X, Jin S, Gan Y, Wang P C, He S, Zhang X and Liang X-J 2012 Size-Dependent Localization and Penetration of Ultrasmall Gold Nanoparticles in Cancer Cells, Multicellular Spheroids, and Tumors in Vivo *ACS Nano* **6** 4483–93

[43] Huo S, Ma H, Huang K, Liu J, Wei T, Jin S, Zhang J, He S and Liang X-J 2013 Superior Penetration and Retention Behavior of 50 nm Gold Nanoparticles in Tumors *Cancer Res.* **73** 319–30

[44] Ménard M, Meyer F, Parkhomenko K, Leuvrey C, Francius G, Bégin-Colin S and Mertz D 2019 Mesoporous silica templated-albumin nanoparticles with high doxorubicin payload for drug delivery assessed with a 3-D tumor cell model *Biochim. Biophys. Acta BBA - Gen. Subj.* **1863** 332–41

SUPPORTING INFORMATION

Design of hybrid protein-coated magnetic core-mesoporous silica shell nanocomposites for MRI and drug release assessed in a 3D tumor cell model

Mathilde Ménard[1,2], Florent Meyer[2,*], Christine Affolter-Zbaraszczuk[2], Morgane Rabineau[2], Alexandre Adam[1], Paula, Duenas Ramirez[1], Sylvie Bégin-Colin[1,*] and Damien Mertz[1,*]

[1]*Institut de Physique et Chimie des Matériaux de Strasbourg (IPCMS), UMR 7504, CNRS, Université de Strasbourg, 23, rue du Loess, BP 43, 67034 Strasbourg, France. E-mails: damien.mertz@ipcms.unistra.fr, sylvie.begin@ipcms.unistra.fr*

[2]*Université de Strasbourg, INSERM, UMR_S 1121 Biomatériaux et bioingénierie, FMTS, 11 rue Humann, 67085 Strasbourg, Cedex, France. E-mail : fmeyer@unistra.fr*

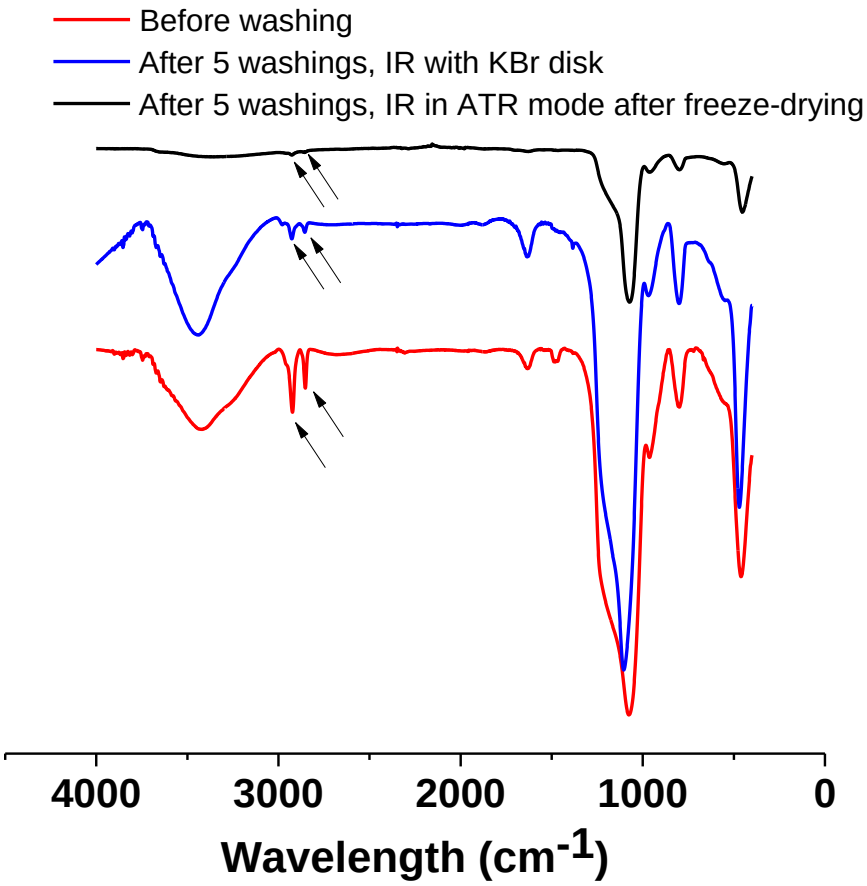

Figure S1. IR spectra of IO@MS NPs before CTAB washing, after 5 nitrate ammonium washings in KBr disks and after 5 nitrate ammonium washings and freeze-drying in ATR mode

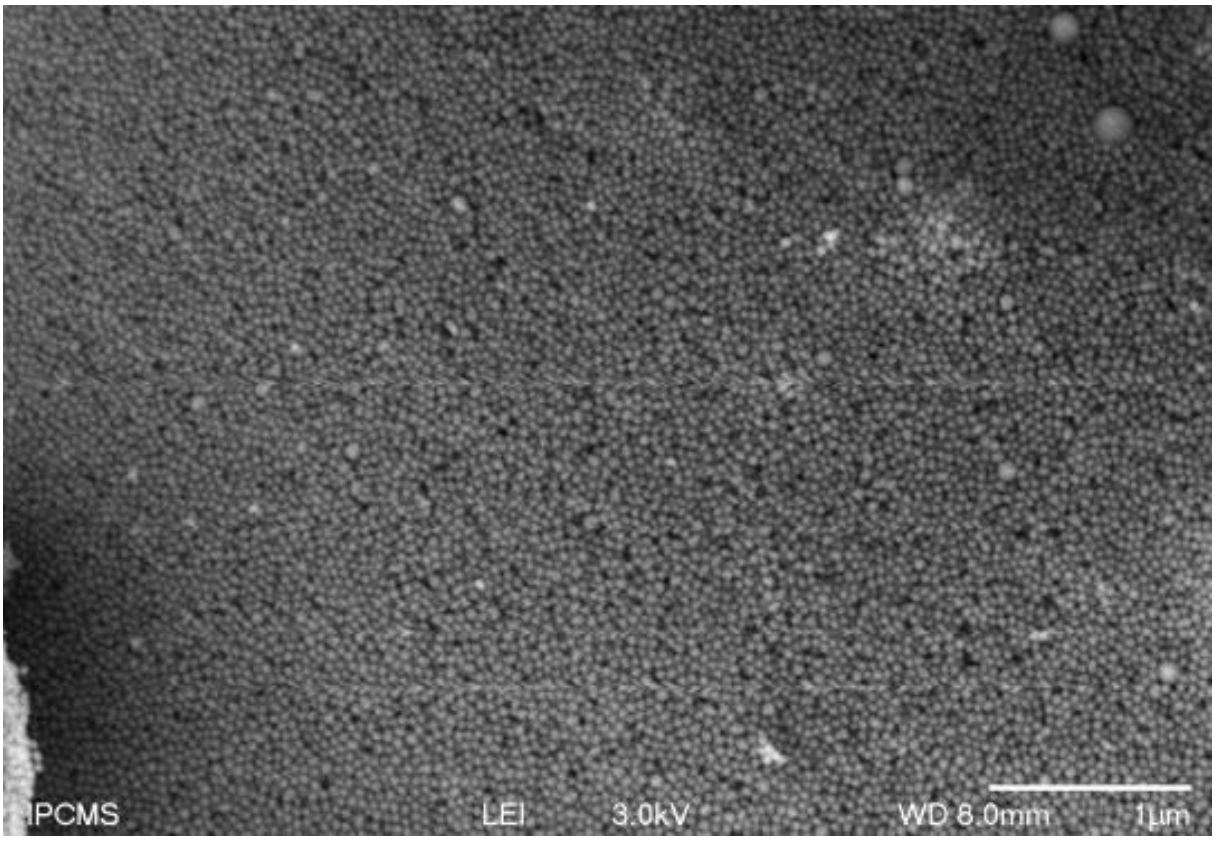

Figure S2. SEM image of the IO@MS NPs.

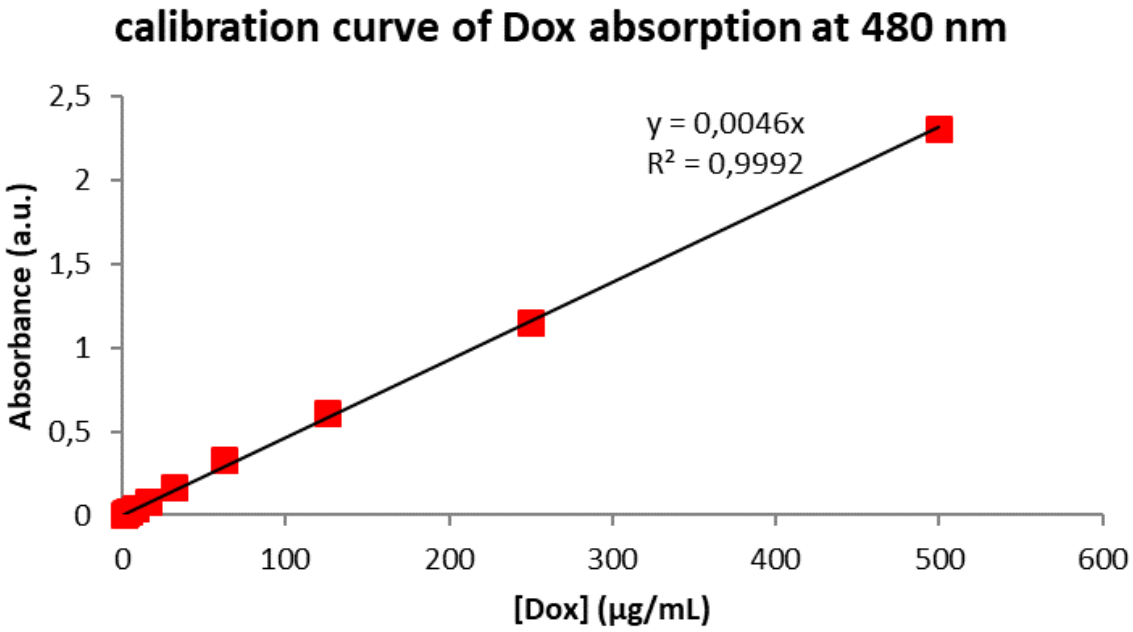

Figure S3. Calibration curves in absorbance for Dox

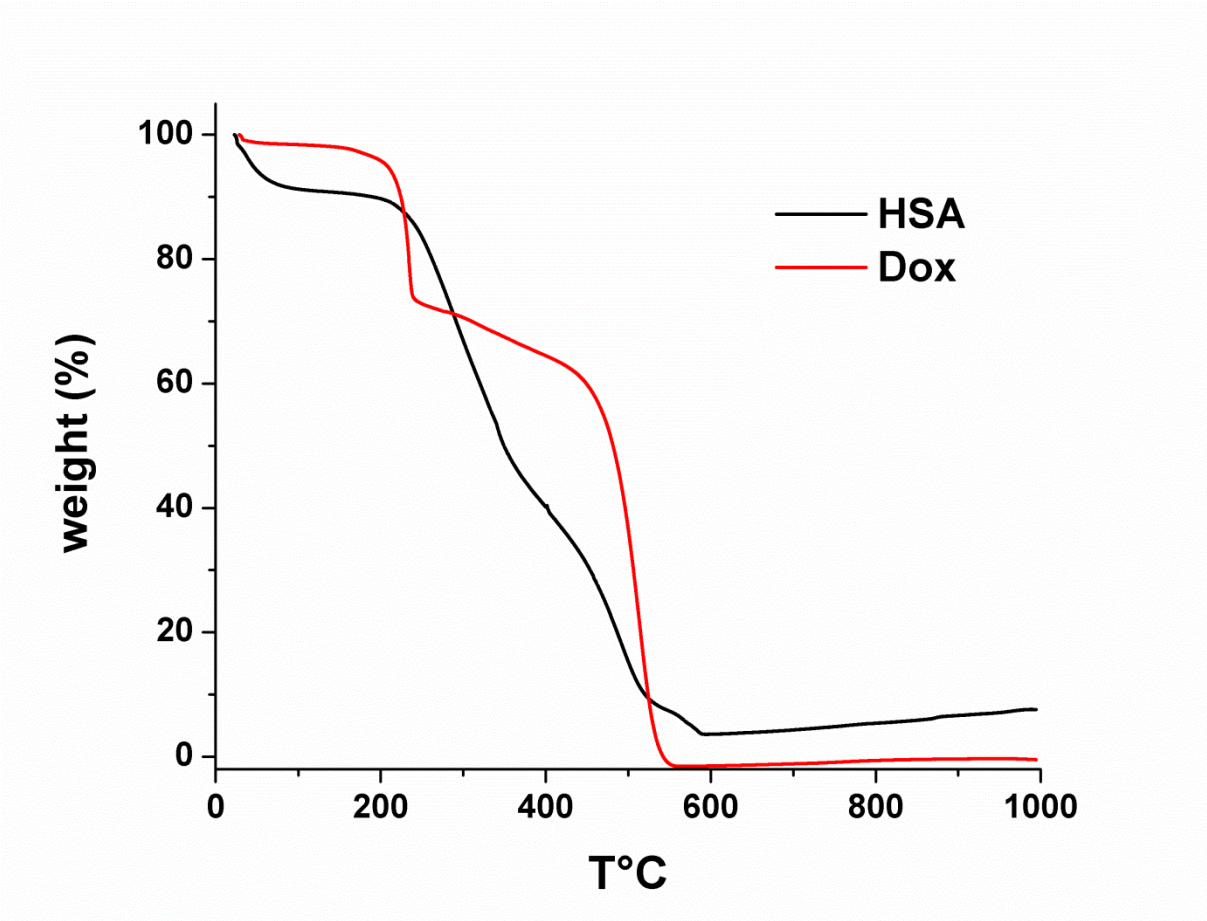

Figure S4. TGA of free Dox and free HSA.

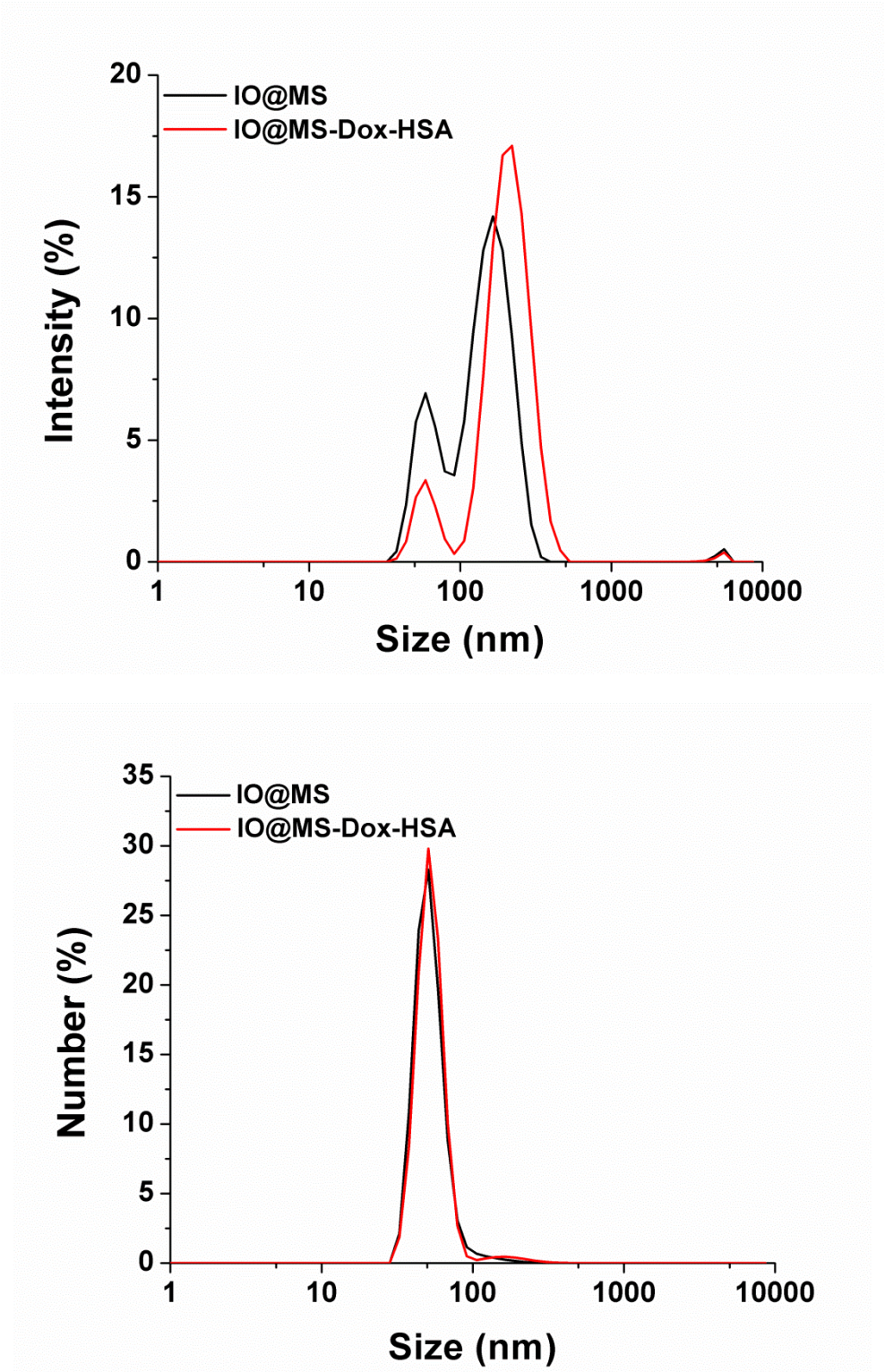

Figure S5: DLS measurement of IO@MS and IO@MS-Dox-HSA in A) intensity an B) number

Figure S6 Picture of the final IO@MS-Dox-HSA NPs dispersed in Milli-Q water

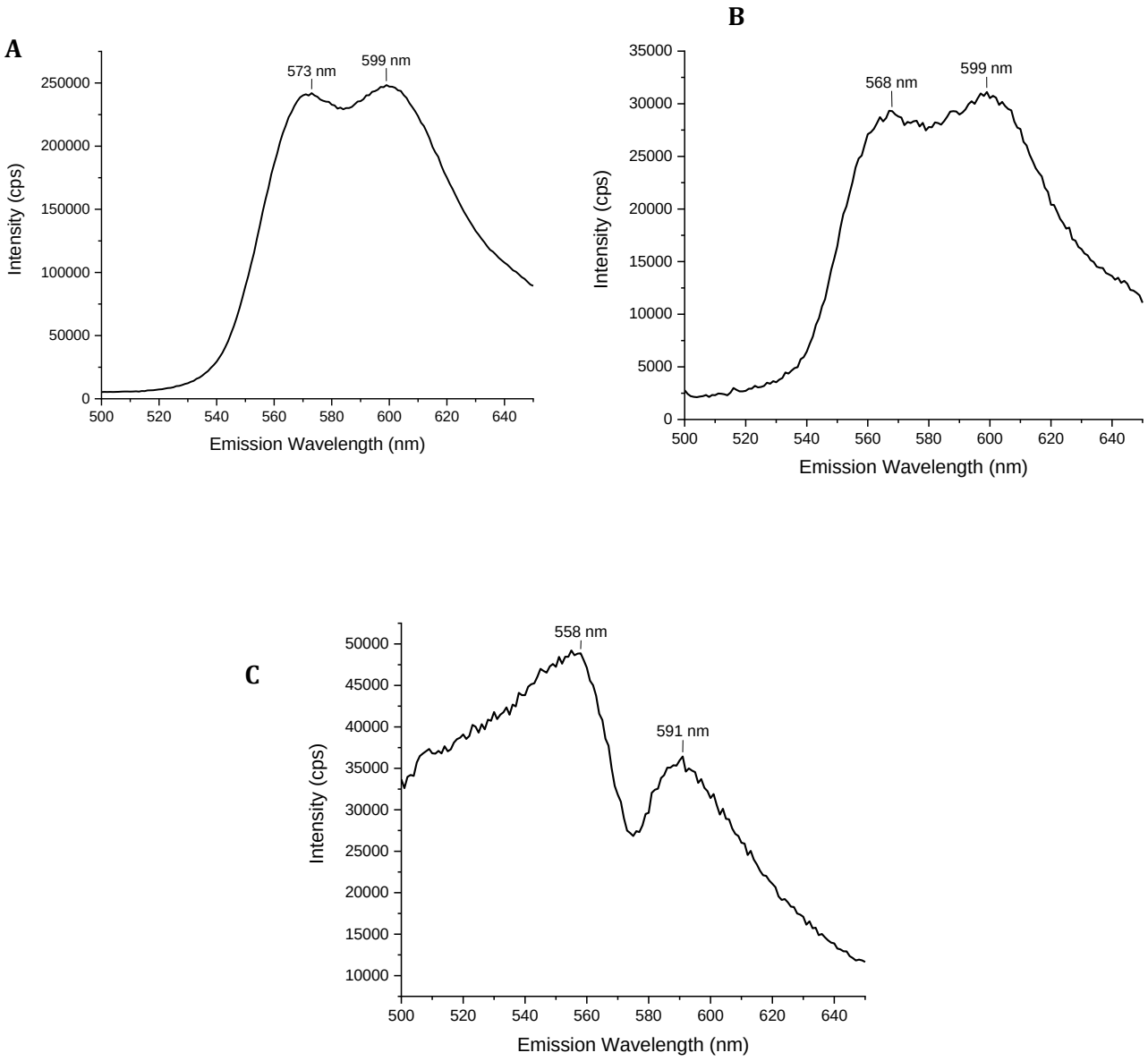

Figure S7. Fluorescence emission spectra (λ_{exc} = 480 nm) of (A) free doxorubicin, (B) IO@MS-Dox and (C) IO@MS-Dox-HSA. All spectra are acquired in distillated water. Each spectrum is shown after subtraction of a blank spectrum. The acquisition of the blank spectrum is performed with the same conditions used for the sample measurement.

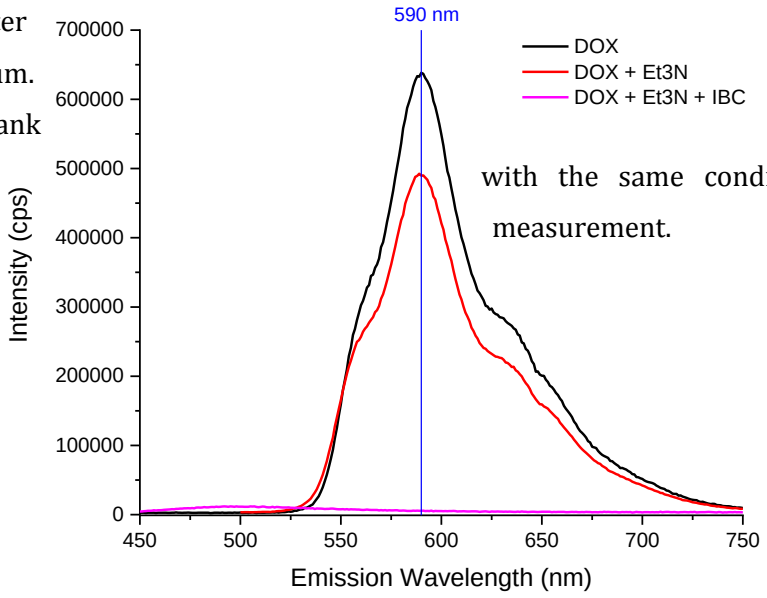

Figure S8. Fluorescence emission spectra (λ_{exc} = 395 nm) of free doxorubicin in DMF and after addition of triethylamine (Et_3N) and addition of isobutyryl chloride (IBC). The addition of Et_3N has no influence on the emission spectrum except the dilution of the sample. On the contrary, the addition of IBC after Et_3N results in the destruction of the fluorescence signal, showing the sensitivity of free Dox to IBC.

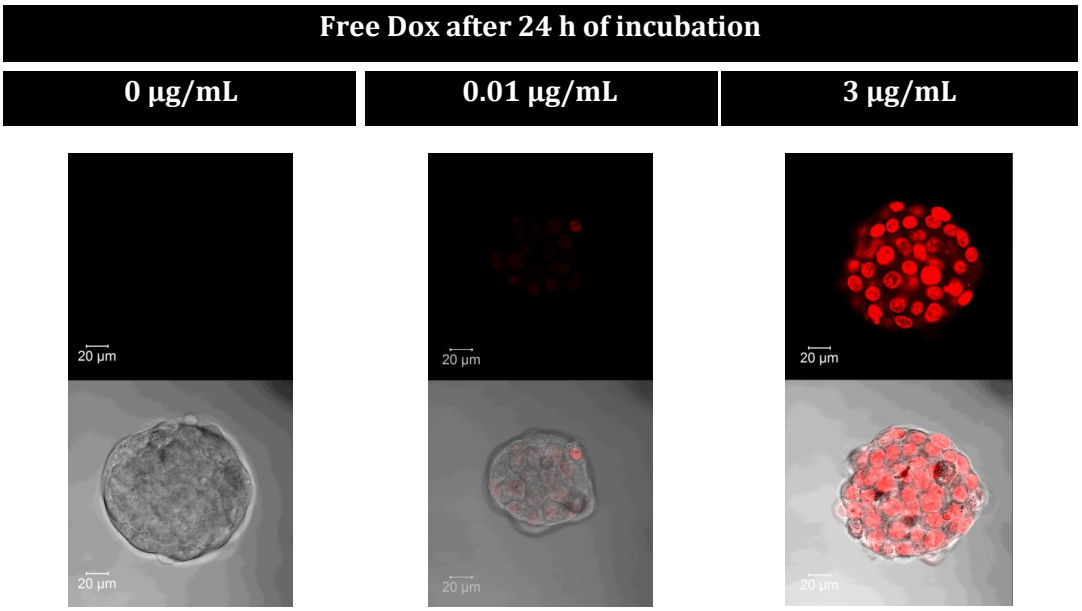

Figure S9. CLSM imaging of free Dox penetration into spheroids after 24 h of incubation at various concentrations: 0, 0.01 and 3 µg/mL.